

Article

Evaluation of Natural Stone Weathering in Heritage Building by Infrared Thermography

Giovanna Pappalardo ¹, Simone Mineo ^{1,*}, Davide Calì ¹ and Annamaria Bognandi ²

¹ Department of Biological, Geological and Environmental Sciences, University of Catania, Corso Italia 57, 95129 Catania, Italy

² Freelance Restoration Technician, Via Musmarra 4, 95024 Acireale (CT), Italy

* Correspondence: simone.mineo@unict.it

Abstract: The application of non-contact diagnostic methodologies is the current challenge in the frame of the cultural heritage, referred to as preservation, monitoring and restoration. Inspired by the potential shown by infrared thermography in rock mechanics' non-destructive applications, this paper presents the results achieved by its use for the quick survey of different weathering types affecting natural stones at historical buildings. Infrared thermography allowed recognizing and mapping the different surface temperatures arising from the presence of efflorescence, subflorescence, alveolization, black crusts and bioweathering at limestone and basalt stones. Infrared data were sided by photogrammetric three-dimensional models of surveyed spots, which provided quantitative data on the thickness of rock affected by mechanical weathering, and key correspondence between the two techniques is highlighted. Achieved results show that infrared outcomes are related to different aspects primarily involving the stone face morphology and color, as well as the environmental conditions at the surveying time. Provided interpretations were validated by field visual inspections, which confirmed the good potential of infrared thermography as a quick weathering diagnostic tool. This study can be therefore considered a starting reference for knowledge development in this scientific field.

Keywords: infrared thermography; photogrammetry; natural stone; weathering



Citation: Pappalardo, G.; Mineo, S.; Calì, D.; Bognandi, A. Evaluation of Natural Stone Weathering in Heritage Building by Infrared Thermography. *Heritage* **2022**, *5*, 2594–2614. <https://doi.org/10.3390/heritage5030135>

Academic Editor: João Pedro Veiga

Received: 27 July 2022

Accepted: 3 September 2022

Published: 6 September 2022

Publisher's Note: MDPI stays neutral with regard to jurisdictional claims in published maps and institutional affiliations.



Copyright: © 2022 by the authors. Licensee MDPI, Basel, Switzerland. This article is an open access article distributed under the terms and conditions of the Creative Commons Attribution (CC BY) license (<https://creativecommons.org/licenses/by/4.0/>).

1. Introduction

Time and atmospheric agents (rain, wind, solar radiation, aggressive atmospheric pollutants, freeze-thaw cycles, crystallization of saline solutions, and growth of organisms) are the main causes of the deterioration of stone materials exposed to external conditions and employed as either construction material or decoration, e.g., [1–3]. Despite the various treatments aimed at preserving the appearance of stones, their weathering represents a serious problem, especially in the preservation of cultural heritage. In particular, the mineralogical composition of rocks, along with their physical properties (with specific regard to porosity), play a key control in the kinetics of degradation processes [3–5]. In the last decade, different non-destructive technologies have been employed to study the deterioration affecting stones at historical monuments and buildings [6–8]. Casula et al. [9] highlighted the presence of cracks and micro-cracks in masonry through the combination of laser and ultrasound scanning techniques, while Avdelidis and Moropoulou [10] used Infrared Thermography (IRT) to detect surface cracks, detachments, differences in material or the presence of moisture within the structures. Nevertheless, the process that leads to the analysis of the problem and to the possible solutions for the restoration and/or conservation of the stone is often long and based on a preliminary visual analysis. Moreover, visual inspections alone may suffer from a non-complete characterization of the problem due to the impossibility of detecting the weathering progress not yet visible to the naked eye. From this perspective, this paper aims to test the potential of IRT applied

for the preliminary evaluation of weathering phenomena affecting natural stones, even in combination with photogrammetry and in situ inspections. The use of IRT on rocks is developed in engineering geological studies for different purposes, such as the laboratory indirect estimation of porosity and the evaluation of the pore persistence [11,12], while in the field, it is widely employed for the characterization of rock masses, e.g., [13–16]. Its use for stone characterization in cultural heritage is still under development, and this research provides a contribution to this field. To test and validate the application of this methodology, IRT surveys were carried out at a historical building located in Catania town (southern Italy). It is Palazzo delle Scienze (PdS), one of the headquarters of the University of Catania, which was built between 1935 and 1942 (Figure 1). As for many other historical edifices built in the late Baroque in the town, its architectural style involves the use of two varieties of rocks: a light-beige limestone and a dark grey igneous rock. Both rock types were largely available at local quarries located at the Hyblean mountains (south of Catania) and Mount Etna. Representative study spots affected by different types of weathering were selected along the external walls and underwent a weathering characterization by means of in situ surveys, photogrammetric 3D models and IRT. Results were compared, aiming to understand the infrared thermal expression of selected weathering types so as to provide an innovative approach for the quick preliminary study of weathering through alternative non-contact methodologies.

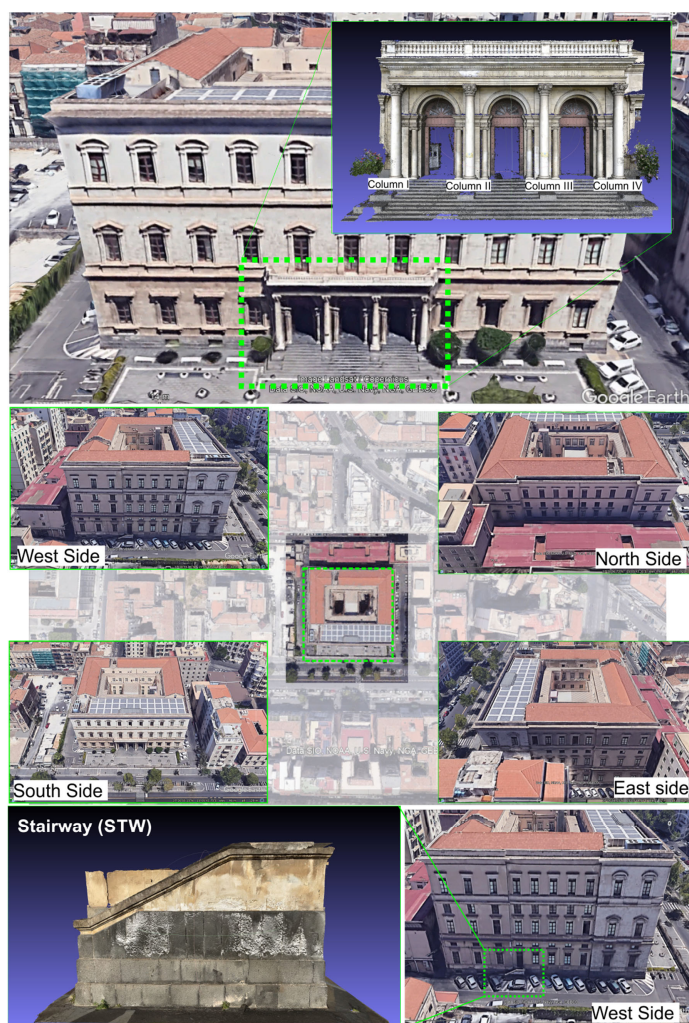


Figure 1. Overview of the Palazzo delle Scienze (PdS) building chosen for this study. Particular elements enclosed in dashed rectangles are 3D models built from photogrammetric dense point clouds and used for the weathering analysis presented herein.

2. Materials and Methods

The stones employed as construction material in the ancient city center of Catania during the eighteenth and nineteenth centuries are both igneous and sedimentary rock types. Their combined use gives rise to a characteristic light-dark duotone in the façades of the buildings [17]. The sedimentary ones are carbonate rocks (mainly limestones), quarried on the Hyblean mountains (south-eastern Sicily) and belonging to different geological formations, while igneous rocks belong to Mount Etna historical or prehistorical lava flows, which can be classified as trachibasalts and trachandesites, e.g., [18,19], with a porphyritic texture and a mineral composition usually represented by plagioclase, pyroxene and olivine in a crystallized groundmass rarely vitrophyric [12]. These are, from now on, generically referred to as “basalts” and can be grouped into two categories according to their texture: massive and vesicular [20]. The methodological approach followed for this research is focused on the laboratory characterization of studied rocks and on the application of remote technologies for the rock weathering identification.

2.1. Laboratory Physical and Mechanical Rock Characterization

Representative specimens of both rock varieties were tested in laboratory with the aim of estimating their main engineering geological properties. Specimens were 70 mm (± 5) cubes, and physical-mechanical tests were carried out according to the EN1926 and EN1936 specifications. In particular, imbibition coefficient (ic), bulk density (γ_b) and total porosity (n) were calculated based on the rock weights in dry (m_{dry}), saturated (m_{sat}) and hydrostatic (m_w) conditions, according to Equations (1)–(3) (where ρ is the water density and γ_r is the rock real density calculated according to the pycnometer method).

Uniaxial Compressive Strength (UCS) and elastic modulus (E) were estimated through compression tests performed by using an automatic 3000 kN hydraulic press machine connected to an E Modulus console for the determination of the elastic modulus.

$$ic = (m_{sat} - m_{dry}) / m_{dry} \quad (1)$$

$$\gamma_b = \frac{m_{dry}}{m_{sat} - m_w} \rho \quad (2)$$

$$n = \left(1 - \frac{\gamma_b}{\gamma_r}\right) 100 \quad (3)$$

2.2. IRT Survey

The IRT technique is based on the principle that every form of matter with temperature above absolute zero emits thermal radiation, whose wavelength mainly falls within the infrared band of the electromagnetic spectrum [21]. This emitted radiation is proportional to the temperature of the emitting body, according to the Stefan–Boltzmann law. Therefore, the surface temperature of an object can be estimated by specific devices called thermal cameras and operating within the range of wavelengths as long as 13–14 μm . Due to the fact that thermal radiation is mainly invisible to the naked eye, IRT represents a useful tool to extend human perception even toward the detection of otherwise invisible phenomena. Thanks to its potential, IRT is currently used in numerous activities and scientific branches also involving the characterization of rocks. In particular, it is applied to the study of rock fracturing in rock masses, e.g., [16,22,23], or for the characterization of intact rock properties and related variations under specific conditions, e.g., [12,24–27]. In the frame of cultural heritage preservation, IRT has already proved useful in detecting biocolonization on natural stones [28], studying sulfated crusts [29] and, more in general, for investigation of chemical degradation processes in historical buildings, e.g., [30–32].

In this paper, IRT images were acquired at selected spots of the PdS building with the aim of framing different weathering types and of shedding light on the corresponding thermal aspect. Surveys were carried out in the absence of direct solar radiation, according to literature experiences [16], during summer and under no rain conditions, by using a high-

sensitivity thermal camera with a 320×240 pixels infrared resolution and a temperature range between -20 and 650 °C (with ± 2 °C accuracy).

Emissivity value was set according to literature data referring to the same rock types [33], namely 0.94 and 0.95 for basalts and limestones, respectively. Thermal images were post processed to highlight specific features according to the different observed weathering types, and results were validated by field inspections.

2.3. Photogrammetric Survey

A photogrammetric digital reconstruction of the building elements surveyed by IRT was carried out with the aim of supporting the analysis presented herein. In particular, 3D models are widely used in the field of cultural heritage [34–36] to generate dense cloud for the analysis of digital models of structural elements. For this study, the acquisition was carried out through photogrammetry, which already showed good results in this field, e.g., [37–39]. Digital images were acquired by a Nikon Z62 digital mirrored camera with a CMOS (Complementary Metal Oxide Semiconductor) sensor of a size (35.9 mm \times 24.9 mm) and a resolution of 6048×4024 px, equipped with a Nikon 24–70 mm lens (Nikon, Tokyo, Japan). Dense point clouds were then postprocessed by a specific tool implemented in the CloudCompare computer program, with the aim of achieving a Digital Elevation Model (DEM) of the analyzed structural elements. This was specifically useful for the study of the stone morphological condition under a specific weathering type (alveolization), with specific reference to the quantitative evaluation of the weathering depth.

3. Physical and Mechanical Rock Parameters

3.1. Hyblean Limestones

Fine-grained limestone quarried at Hyblean Mountains (Figure 2a,b) shows a porous texture given by millimetric voids. Their total porosity, generally related to primary processes, is, on average, around 37.65%, and most of it is represented by interconnected voids, which confer the rock an average effective porosity of around 27%. Their bulk density ranges from 1501 to 1850 kg/m³, and the degree of compactness, expressed by the ratio between real and bulk densities, is between 1.43 and 1.79 (Table 1). In this case, real density was calculated according to the pycnometer method (Figure 2c). Uniaxial compression tests (Figure 2d) highlighted a wide range of strength values (Table 1). In particular, the most porous specimens are characterized by lower UCS and E values, suggesting a control played by porosity on the mechanical behavior of these rocks. Such properties are statistically well correlated, with specific reference to UCS, E and porosity. In particular, by plotting UCS against porosity (Figure 2e), a negative linear statistical correlation with a 0.81 determination coefficient (r^2) is outlined. It proves the strong dependence between the rock strength and porosity, according to several literature experiences, e.g., [40,41]. On the other hand, UCS and E are statistically correlated by a positive linear relation (r^2 0.75) (Figure 2f), suggesting that the highest strength corresponds to lower deformability of intact rock, similarly to other published experiences, e.g., [42,43].

Table 1. Estimated physical mechanical parameters of hyblean limestones (HL).

ID Specimen	Bulk Density (kg/m ³)	Degree of Compactness	Imbibition Coefficient (%)	Effective Porosity (%)	Total Porosity (%)	Elastic Modulus (GPa)	UCS (MPa)
HL1	1516	1.77	21.2%	32.1%	43.6%	1.4	6.99
HL2	1523	1.76	21.0%	32.1%	43.3%	1.5	7.17
HL3	1501	1.79	21.4%	32.2%	44.1%	1.2	6.74
HL4	1586	1.69	18.8%	29.9%	40.9%	2.2	9.82
HL5	1529	1.76	20.7%	31.7%	43.1%	1.2	8.59
HL6	1635	1.63	18.2%	29.8%	38.7%	3.6	11.40
HL7	1651	1.62	18.0%	29.8%	38.1%	2.1	8.93
HL8	1754	1.52	14.5%	25.4%	34.3%	2.8	13.41
HL9	1635	1.64	18.4%	30.2%	39.0%	2.9	6.71

Table 1. Cont.

ID Specimen	Bulk Density (kg/m ³)	Degree of Compactness	Imbibition Coefficient (%)	Effective Porosity (%)	Total Porosity (%)	Elastic Modulus (GPa)	UCS (MPa)
HL10	1850	1.43	11.3%	20.9%	30.0%	4.7	24.54
HL11	1817	1.46	12.3%	22.4%	31.3%	4.6	14.64
HL12	1790	1.48	13.0%	23.3%	32.5%	4.1	20.16
HL13	1836	1.44	11.6%	21.3%	30.6%	5.2	22.05
<i>mean</i>	1663	1.61	16.9%	27.77%	37.65%	2.9	12.40
<i>min</i>	1501	1.43	11.3%	20.9%	30.0%	1.2	6.71
<i>max</i>	1850	1.79	21.4%	32.2%	44.1%	5.2	24.54

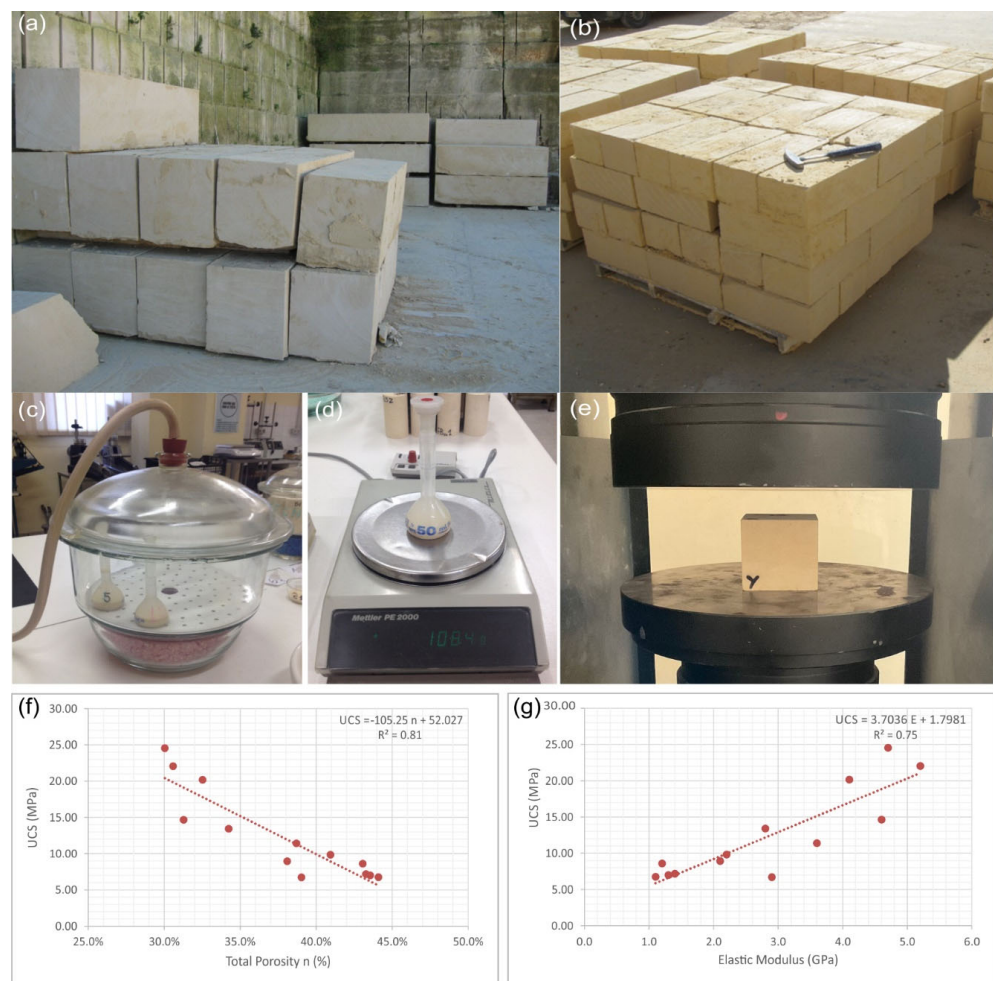


Figure 2. (a,b) Limestone blocks at the sampling quarry; (c,d) a photo taken during the pycnometer analysis for real density estimation process; (e) representative basalt specimen in the hydraulic press before uniaxial compression test; (f) statistical regression between UCS and total porosity; (g) statistical regression between UCS and E.

3.2. Etna Basalts

On the other hand, massive basalt samples were taken at a quarry located on Mount Etna (Figure 3a) and show a macroscopic massive structure with no visible voids (Figure 3b). Their laboratory characterization (Figure 3c,d) returned good mechanical properties, with UCS mean values around 210 MPa. Literature reports a wide statistical range of this parameter in basalts, which is often influenced by specific rock features, such as the presence of cracks [12,20]. The total porosity of tested rocks is low (on average 4.7%), and voids are represented by both microvoids, often isolated, and microcracks. Unlike limestones, the

degree of compactness of selected basalts is 1.05 (Table 2) due to the massive structure of the rock. Statistical regression analysis of selected parameters returned satisfactory correlations. For example, UCS and porosity are linked by a negative linear law, although tested rocks' porosity is comprised within a narrow statistical range (Figure 3e). A similar consideration can be reported for the relation between UCA and E, affected by a positive linear trend (r^2 0.64) (Figure 3f).

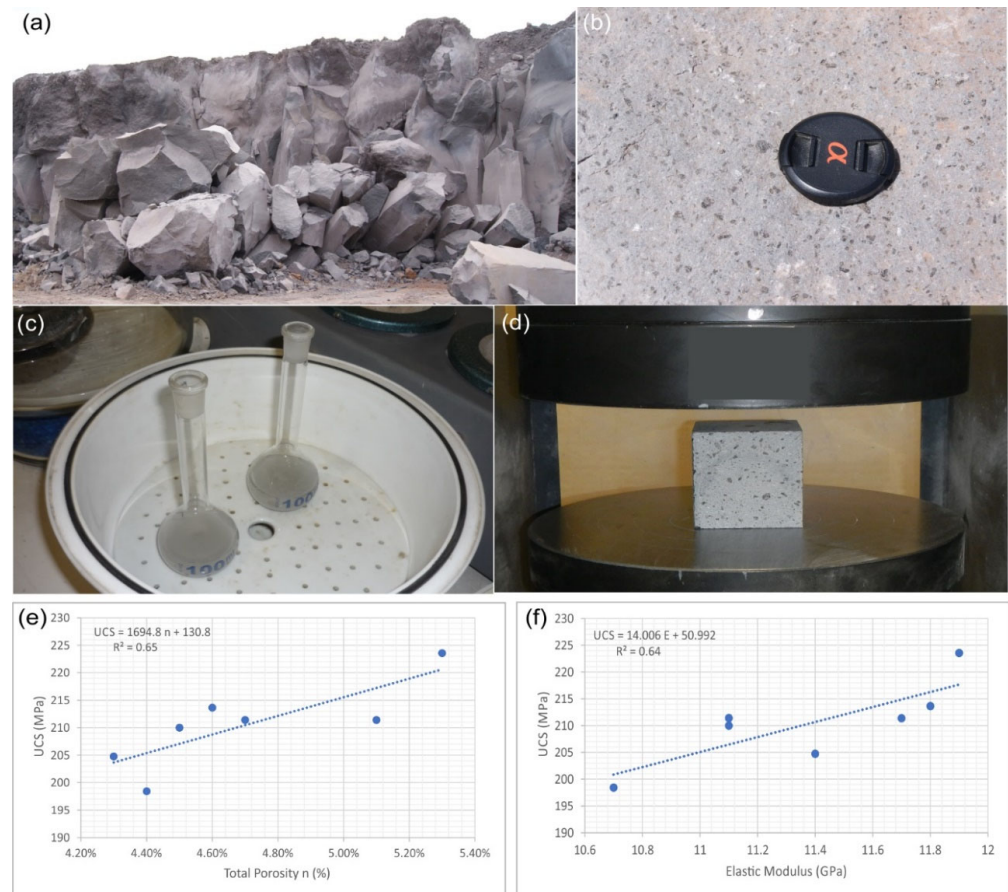


Figure 3. (a) Sampling quarry of Etna basalts; (b) particular of the macroscopic appearance of a massive basalt; (c) a photo taken during the pycnometer analysis for real density estimation process; (d) representative basalt specimen in the hydraulic press before uniaxial compression test; (e) statistical regression between UCS and total porosity; (f) statistical regression between UCS and E.

Table 2. Estimated physical mechanical parameters of etna basalts (EB).

ID Specimen	Bulk Density (kg/m ³)	Degree of Compactness	Imbibition Coefficient (%)	Effective Porosity (%)	Total Porosity (%)	Elastic Modulus (GPa)	UCS (MPa)
EB1	2815	1.052	10.0%	2.8%	5.1%	11.1	211.40
EB2	2837	1.050	9.4%	2.7%	4.5%	11.1	210.00
EB3	2814	1.052	10.3%	2.9%	5.3%	11.9	223.56
EB4	2845	1.050	9.2%	2.6%	4.6%	11.8	213.63
EB5	2838	1.049	10.8%	3.1%	4.4%	10.7	198.44
EB6	2831	1.052	10.5%	3.0%	4.7%	11.7	211.39
EB7	2841	1.051	8.8%	2.5%	4.3%	11.4	204.76
<i>mean</i>	2832	1.051	9.9%	2.8%	4.7%	11.4	210.45
<i>min</i>	2814	1.049	8.8%	2.5%	4.3%	10.7	198.44
<i>max</i>	2845	1.052	10.8%	3.1%	5.3%	11.9	223.56

4. Observed Weathering Types

In this section, results related to the observed forms of weathering along the two lithotypes at PdS are presented. The description provided in this section, differentiated by weathering type, is based on in situ surveys aimed at describing the main features occurring along the selected spots. In particular, four types of weathering phenomena have been observed: (1) efflorescence and subflorescence, (2) alveolization, (3) black crust and (4) bioweathering. The first type was surveyed at both lithotypes, while alveolization, black crusts and bioweathering were reported at limestones.

4.1. Efflorescence and Subflorescence

The chemical weathering of rocks is a spontaneous and irreversible process leading the affected material towards a more stable state under a given temperature and pressure conditions [44]. Among the chemical weathering processes, efflorescence is caused by deposited salts crystallizing. After that, a solution migrates through the rock and then evaporates. These minerals are generally sulfates and carbonates of sodium, potassium, or calcium, as well as nitrates and chlorides. In particular, the role of salts in rock weathering has been recognized during the last decades, both in natural areas and in monuments [45–47]. The salts act not only as a physical force but also as saline solutions, which facilitates the dissolution rates of silicate minerals [45]. Since this process arises from the migration of water through the rock, its occurrence suggests water infiltration phenomena and related consequences. In fact, saline efflorescence may cause the haloclastic rupture of affected materials, being a serious issue not only in construction and decorative stones, e.g., [48], but also for masonry, underground construction, e.g., [49], and natural environments, e.g., [45]. With reference to natural stones employed as construction material, the overpressure generated by salt crystals causes the exfoliation of the rock through a progressive detachment of the shallowest rock portions. More specifically, the results of salt crystallization and precipitation under the surface of a material causing spalling, sugaring, flaking and/or pitting is acknowledged as subflorescence. Whereas efflorescence is relatively easy to remove, the subflorescence is difficult as it is formed below the rock surface [50].

Among the PdS elements chosen for this study, this weathering form was found at both the igneous rock, used as cladding along the lower part of the façade and as column stereobate along the south-facing prospect of the building, and at limestones occurring along the façade and used as column stylobates. With respect to the igneous rock type, we found some differences according to the building façade exposure: the most affected sector faces north, where the igneous rock spalling and flaking is deeply developed (Figure 4a,b). Evidence of efflorescence was found both at the bared inner rock portion and at the most external weathered and loose rock sheet (Figure 4a); in this case, the rock thickness affected by mechanical and chemical weathering is maximum. Along the west-facing façade, evident signs of efflorescence are visible at the igneous rock strip also bordering the stairway of a secondary entrance to the building, from now on referred to as STW. This structural element protrudes with respect to the PdS main structure, being more exposed to the atmospheric weathering agents (Figure 4c). In this spot, we could also evaluate a sort of evolution of the mechanical rock flaking, testified by different layers of flaked rock sheets that we numbered according to progressive orders starting from the unflaked rock face (Figure 4d). This testifies to the subflorescence progression within the inner rock through different flaking stages.



Figure 4. Efflorescence phenomenon and subflorescence effects observed at the igneous rocks employed as cladding along the lower part of the north-facing façade (a,b), STW (c,d), and as column II and III stereobates along the south-facing prospect of the building (e,f).

The evidence of efflorescence and subflorescence is also reported along the colonnade, with specific reference to the basaltic stereobates (Figure 4e,f), where there is an advanced state of deterioration (flaking order II). Signs of efflorescence occur within the studied element, both at the exfoliated rock portions and at unflaked spots. In this latter case,

salt deposits are also found aligned along borders, representing the potential detachment margin of the ongoing rock flaking.

Efflorescence phenomena also affect the limestone rock type, although in this case, it is combined with other weathering types, such as alveolization, which is discussed in the following sections (Figure 5).

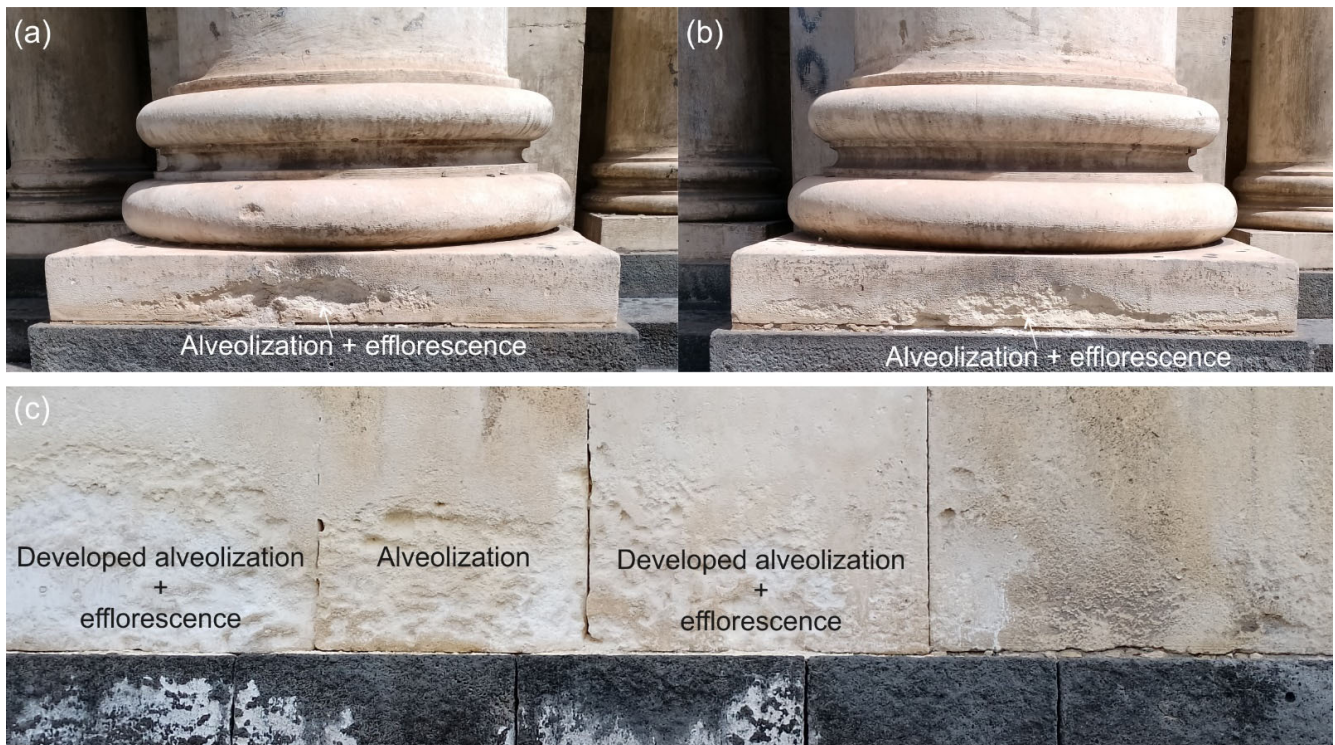


Figure 5. Alveolar weathering and slight efflorescence observed at the carbonate stylobates of two columns II (a) and III (b) and along STW (c).

4.2. Alveolar Weathering

Alveolar or honeycomb weathering is a kind of differential weathering phenomenon developing as a result of a number of different weathering processes involving soluble salts in most cases [51], granular disintegration and/or scaling. Its expression on natural stones is the widespread presence of visible cavities (alveoli) variable in shape and size. In particular, pressures generated by salt crystallization, arising from supersaturated solutions percolation through the rock, are a major cause of the physicochemical weathering of rock structures [52] and references therein. This phenomenon is stressed by the abrasive effect played by rock incoherent grains, taken over by turbulent air currents, which contribute to enlarging the cavity size.

In this case study, alveolar weathering is well developed in the limestone rocks used for both the upper façade and for the colonnade. Due to their porosity grade and low mechanical strength, this lithotype is a common candidate for this weathering process, as testified by literature studies on rocks belonging to the same geological setting, e.g., [53,54], and, more generally, on carbonate rock types worldwide, e.g., [51,55,56]. Nevertheless, the presence of alveoli is localized to specific portions of both the façade and columns. In the first case, they are found immediately above the basal band of basalt, with specific reference to STW (Figure 5a), while in columns, they occur at the stylobate (Figure 5b,c). In both cases, the underlying basalt stone is more protruding, thus offering a basis for the bounce of rain water droplets, which enhances the mechanical limestone disaggregation. The evolution of such weathering process can be recognized by the morphological definition

of alveoli, which tend to coalesce as the weathering develops, leading to the formation of wide deteriorated sectors (Figure 5c).

4.3. Weathering from Air Pollution and Biological Activity

The weathering arising from air pollution on carbonate stones is expressed by black crusts. Their formation originates from a sulfation reaction (SO_2 reacts with calcite to form gypsum), and the entrapment of particles (especially soot) causes its blackening [57–59]. This phenomenon is well acknowledged in the literature, as it largely affects heritage in urban environments thanks to the capability of atmospheric pollutants to form compounds that can interact with building materials. The degradation products are visible on calcareous building materials, e.g., [60,61], especially in sheltered sectors, preserved from washing action. Gypsum, indeed, is soluble in water, and it is usually washed away. Black crust evolution leads to a progressive thickening and a rock porosity reduction. Moreover, the black color favors heat absorption more than the surrounding light color rock, enhancing mechanical dilatation phenomena, which progressively weaken the mechanical attitude of the rock itself until its gradual disintegration. At PdS, black crusts were surveyed at the upper portion of STW (Figure 6a), at the hollow portion between the column toruses, and at some sheltered façade spots, such as those below the window sills (Figure 6b).

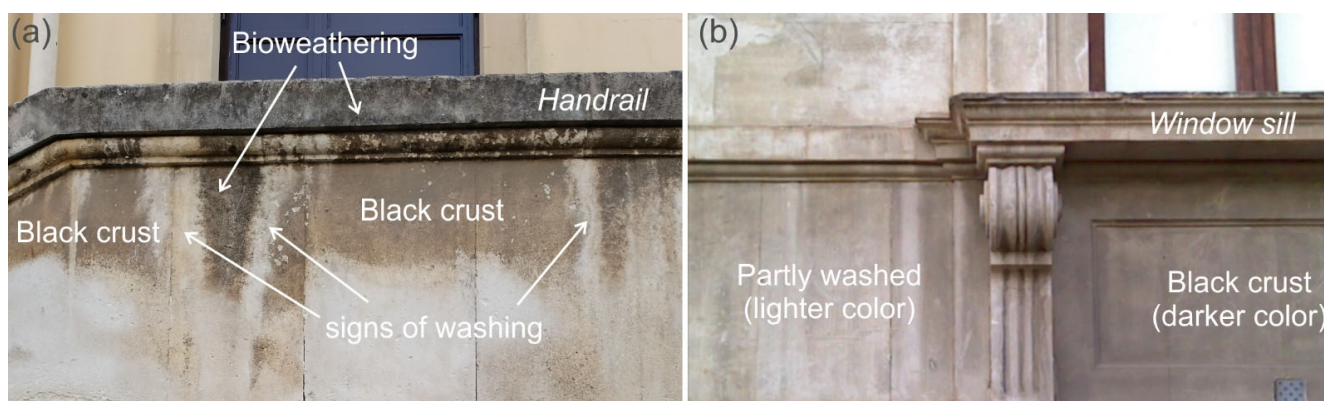


Figure 6. (a) Focus on the limestone wall at STW, affected by black crust and bioweathering; (b) particular of the PdS façade showing the chromatic difference between the washed and the sheltered façade portions.

Bioweathering, on the other hand, occurs when the employed stone becomes subject to colonization by microorganisms [62]. Among the biodeteriogens, the most widespread are microscopic algae and lichens, which may implant on porous or deteriorated rock surfaces, penetrating between already detached fragments. On light-color rocks, their colony occurs as a darker film, especially localized in damp sectors. Evidence of bioweathering was surveyed at STW, with specific reference both to the handrail, exposed to wetting and absorption of meteoric water, and to a localized spot along the vertical limestone wall subject to water flow (Figure 6a).

5. IRT Survey

In this section, results arising from IRT application to the survey of the afore-described weathering types are presented.

5.1. IRT Applied to Efflorescence and Subflorescence

The infrared images related to the basaltic rocks taken into account herein show that efflorescence phenomena can be detected by IRT due to a different surface temperature owned by affected sectors with respect to the surrounding rock portions. With reference to column stereobates, the analysis of IRT images highlighted a surface temperature varying according to specific features occurring within the framed area. In column III (Figure 7a),

for example, surface temperature ranges from 32 to 35 °C suggesting a sort of thermal non-uniformity of the rock, even considering that no direct radiation was affecting the framed elements at the time of the survey. Starting from a general overview (Figure 7a), a clear distinction between warmer and colder sectors can be described. Warmer sectors are found where the igneous rock shows a lower degree of weathering, namely at those exposed rock portions that are not affected by efflorescence and which could have also been bared by flaking phenomena (Figure 7b). Contrarywise, colder temperatures are found at the loose rock portions, which have already been partially detached by subflorescence phenomena, and are represented by rock slices more exposed to environmental cooling (Figure 7c). The correspondence between such thermal outcomes and the state of the rock material was verified in the field. In fact, the loose rock slice occurring at the upper-left side of the column III stereobate is recognizable even to the naked eye. Nevertheless, by observing the thermal image (Figure 7a–c), the cold area is much wider than the visible weathered rock slice. This suggests that the rock portion labeled by the negative thermal anomaly (cold region) has already been detached by its sub-stratum. This should be regarded as a flaking expansion area in the frame of weathering evolution monitoring or forecasting. Further cold sectors are found at the upper stereobate corners, with specific evidence on the right side. Although the cold corner is also an effect of the rock cooling process, as suggested by literature studies [63], the cold anomaly labeling the right edge of the stereobate could be thought of as an index of a loss of adhesion of the rock to the substratum; this phenomenon occurs, even though with a slighter thermal anomaly, also at the opposite side. Finally, intermediate surface temperatures (Figure 7d) correspond to rock portions affected by a slight saline crystallization film, providing an indication of the progression of the considered weathering phenomenon. For column II (Figure 7e), similar considerations can be provided. In particular, a thermal contrast between the upper and lower rock sector is outlined, highlighting that weathering is heavier at the upper stereobate portion. More specifically, by filtering the image considering only the highest surface temperature range (Figure 7f), indicating the sound rock, it is possible to state that the stone degradation progresses from top to bottom. The lowest surface temperatures were found at the partially flaked rock slices, and the flaking expansion sectors can be recognized (Figure 7g). Intermediate surface temperatures (Figure 7h) show that the deposition of salt crystals is widespread, with a specific concentration at the hollow rock surface parts, which arise from the bush hammered finish of the stone. Moreover, signs of efflorescence are found at both the rock bared by occurred flaking and at the portions surrounding the stone slices still in place.

By analyzing the basaltic cover around STW (Figure 8a), the above considerations find a positive correspondence. In particular, the rock flaking process can be recognized due to the thermal contrast occurring between a sound rock (warm surface temperatures) and detached slice (cold surface temperatures) (Figure 8b). The colder region allows also bordering the flaking expansion area, which cannot be easily mapped only by a naked eye observation. Moreover, the wide efflorescence spots located along the basaltic wall hold the lowest recorded temperatures, suggesting a certain thickness of deposited salts (Figure 8c). This feature can be observed even to the naked eye, although IRT image shows that the colder regions are not related only to the presence of salts but also to the occurrence of moisture originating from the contact fissures between stone slabs and with a clear ascent path from the bottom to the top of the stone strip. Even in this case, the intermediate temperatures are related to those rock portions hosting even slight efflorescence signs. A further note is that the negative, horizontal, linear anomaly occurring between the two orders of basaltic strips is only related to the fact that the lower order is more protruding than the one above, thus providing a quicker cooling of the specific rock portion.

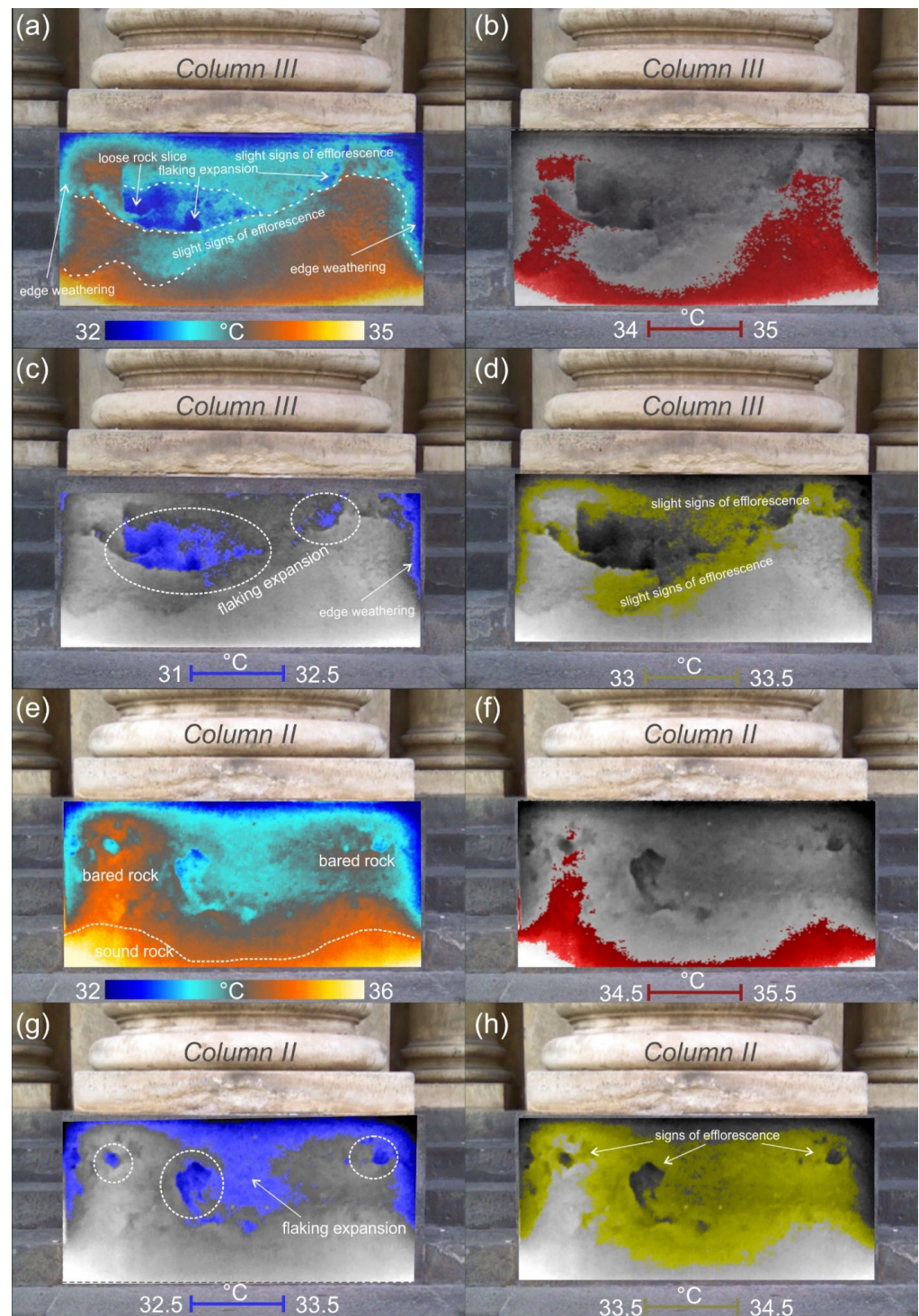


Figure 7. Thermal IR image of basaltic column stereobates overlapped with a digital image of the same element. Column III: general thermogram (a), highest surface temperatures (b), lowest surface temperatures (c) and intermediate surface temperatures (d); column II: general thermogram (e), highest surface temperatures (f), lowest surface temperatures (g) and intermediate surface temperatures (h).

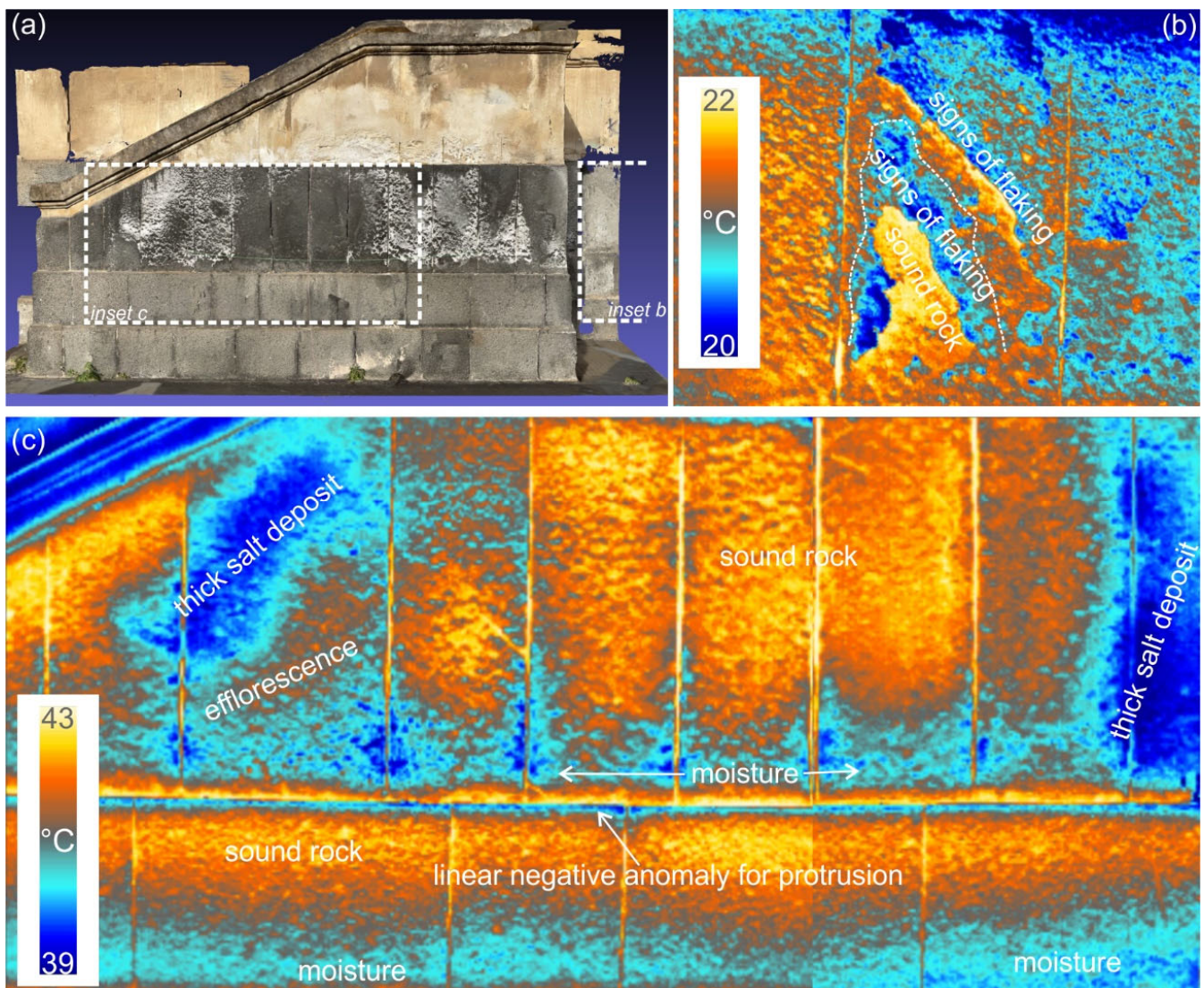


Figure 8. Thermal IR image of basaltic cover occurring along STW (a); thermal image of a particular area affected by flaking phenomena (b); thermal image of the basaltic strips affected by efflorescence and moisture (c).

5.2. IRT Applied Alveolization

For the infrared study of alveolization, IRT analysis was aided by the 3D photogrammetric evaluation of the surface stone morphology. In particular, three-dimensional digital models of column stylobates and STW were analyzed. As previously stated, alveolar weathering affects the limestone rock portions immediately overlying a protruding element, which in this case, is represented by basaltic rock. All the column stylobates are affected by such weathering process, as testified by both visual inspection and the 3D model. In particular, the alveoli presence prevails in the central portion of the stylobate, and their maximum horizontal depth is around 1.4 cm (Figure 9). The IRT expression of hollow rock portions, when framed under no direct irradiation, is a warm surface temperature, according to literature experiences, e.g., [64–66]. This is because the hollow morphology prevents the rock from cooling if compared to the surrounding rock portions more exposed to the external environment. In this case, IRT images highlight that alveoli are labeled by the warmest temperatures, retracing the cavities highlighted by the 3D model, although when a salt crystallization film occurs within the alveolus, its surface temperature is lowered (Figure 9). Moreover, if subflorescence occurs enough to lead to detachment of rock slices,

the rock surface temperature is even lower (Figure 9). Moisture at the upper corners of stylobates is present even in this case, as previously observed at the basaltic stereobates, and it affects the whole upper part of the structural element, thus suggesting the upper origin of water infiltration.

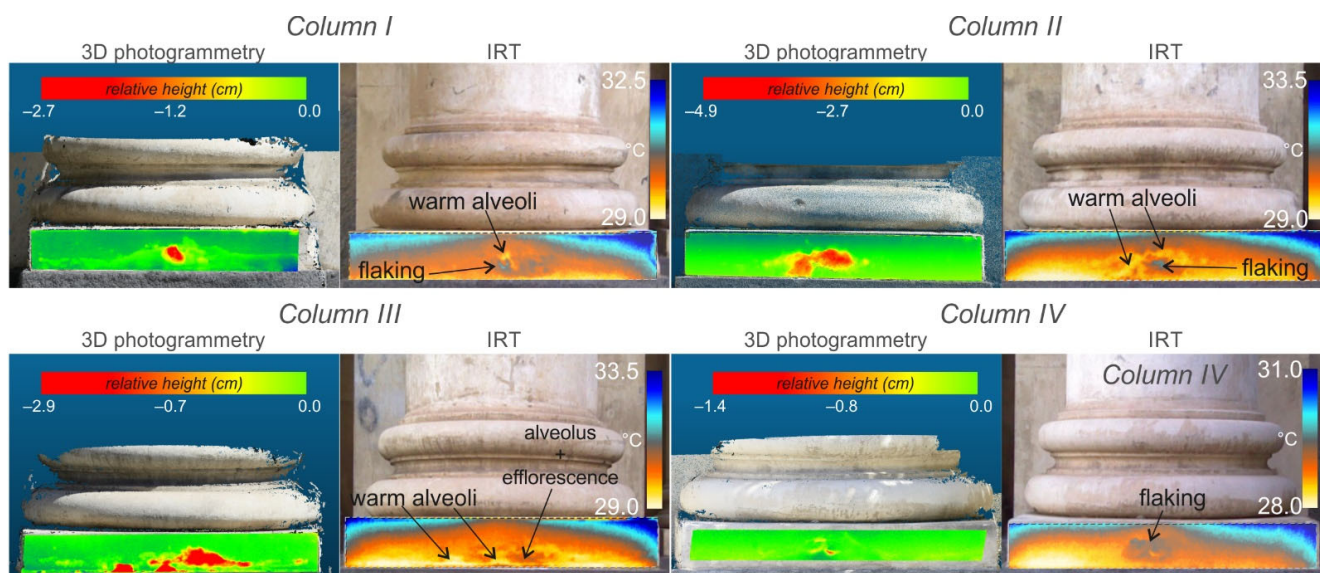


Figure 9. Alveolar weathering at column limestone stylobates. Comparison between 3D digital model postprocessed to evaluate the relative horizontal depth of alveoli and IRT image (this last overlapped to a digital photo).

At STW, the heaviest weathering is represented by alveolization and efflorescence, with consequent flaking due to subflorescence (Figure 10a). In particular, alveolar weathering shows signs of an advanced process, with a heavy mechanical disaggregation of rocks. In fact, wide eroded areas, rather than a purely alveolar structure, locally occur with a developed alveolization and efflorescence, with a maximum horizontal depth of about 2 cm (Figure 10b). This affected part is located over the basaltic strip, which favors, as previously stated, the rain droplet rebound, thus enhancing the mechanical rock weathering. The thermal image of this portion (Figure 10c) shows a prevalence of low surface temperatures, with the lowest values (about 29.5 °C) found where alveolization and efflorescence coexist. On the other hand, alveoli alone are characterized by the highest surface temperature (30.5–31.0 °C) due to their hollow morphology (Figure 10b), according to what was observed in columns. In this case, flaking portions have a slightly higher surface temperature than the surrounding area with efflorescence.

The weathering process evolves upwards into efflorescence (surface temperature between 29.7 °C and 29.9 °C), while the highest temperatures found at the upper STW portion are related to other weathering types, namely black crusts and bioweathering, which are discussed in detail in the following section.

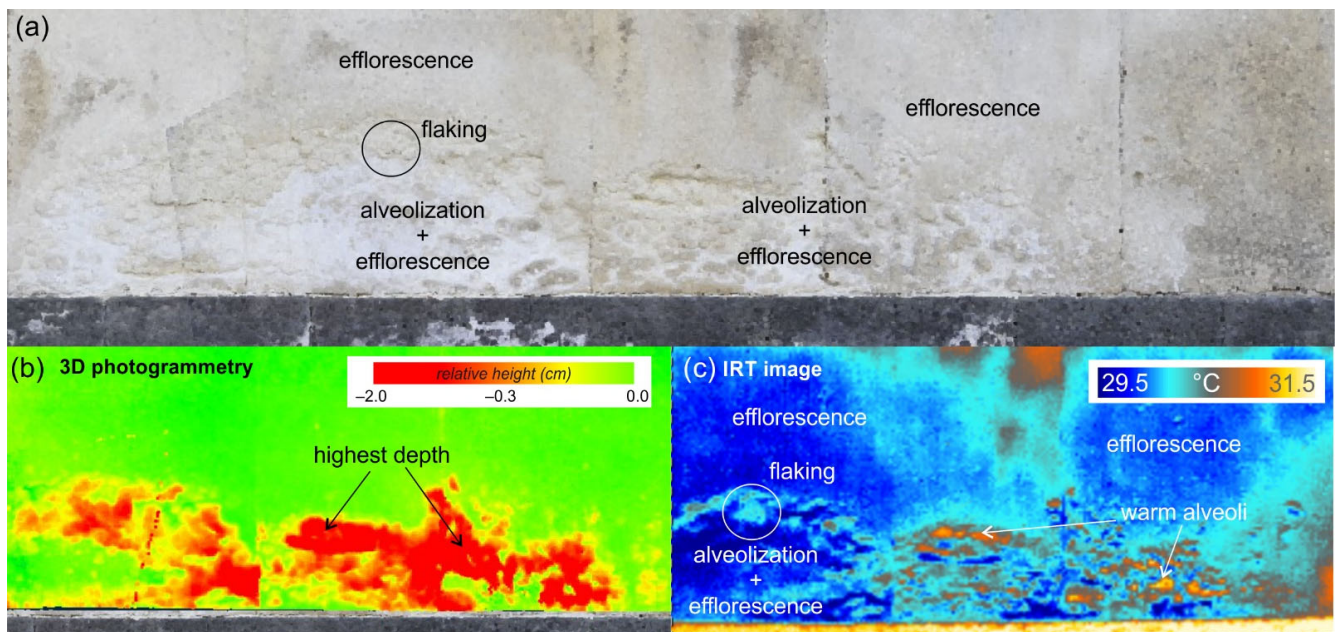


Figure 10. (a) Limestone wall at STW (digital model); (b) evaluation of the horizontal depth of alveolar weathering on 3D model; (c) IRT image highlighting the thermal aspect of alveolar weathering.

5.3. IRT Applied to Black Crust and Bioweathering

The post-processing of infrared images acquired at STW and at a selected spot of the PdS façade allowed carrying out some consideration even with respect to the presence of black crust and bioweathering. In particular, the occurrence of black crust can be identified by IRT thanks to the chromatic difference existing between the crust and the washed limestone, leading to dissimilar heat absorption. This can be well observed by IRT during the rock cooling when images are acquired under no direct solar radiation (such as after sunset or in shadow conditions). In this case, black crusts occurring at the stairway (Figure 11a) wall are labeled by the highest surface temperatures (30.7–31.0 °C), while the washed, light-colored rock keeps a lower surface temperature (30.0–30.2 °C). Consistent results were achieved by analyzing and comparing the thermal outputs of an exposed façade portion and a close part below a window sill, sheltered from rain washing (Figure 11b). In this case, the warmest temperatures were found where the rock was affected by a black crust cover, while intermediate surface temperatures were found at washed rock and the lowest values at rock parts affected by efflorescence, in accordance with afore provided results. Just a note on Figure 11b: the colder region occurring right below the window sill likely originated from the shadow effect played by the column capital, which prevented this part from direct insolation before the survey.

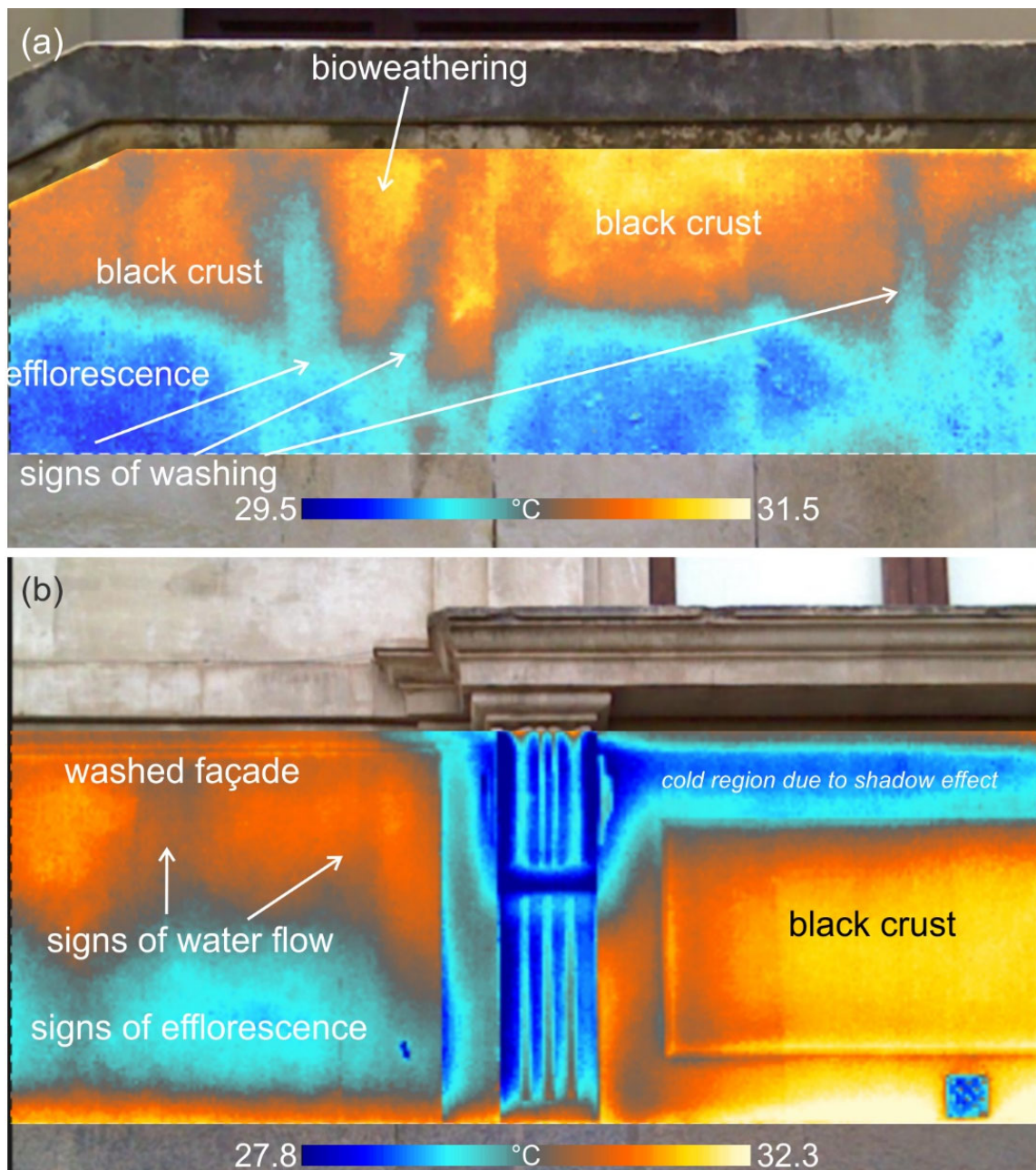


Figure 11. (a) Post-processed IRT images of STW overlapped to a digital photo of the stairway showing the different types of weathering recognized; (b) post-processed IRT image of a façade portion overlapped to the corresponding digital photo showing the thermal difference between exposed and sheltered façade portions.

Similarly, the bioweathering dark crust occurring along the wall, specifically located where signs of water flow were surveyed (Figure 11a), shows high surface temperatures (about 31 °C). This is due to the similar thermal behavior arising from the similar color owned by these two types of weathering. In this case, a differentiation based only on IRT could represent a challenge, although it must be underlined that this survey was carried out during the dry season, and no rainfall had occurred in the weeks preceding the survey.

6. Discussion and Conclusions

Results arising from the surveying methodological approach presented in this paper show that Infrared Thermography (IRT) represents a useful non-contact tool to be employed

in the quick preliminary evaluation of the weathering state of natural stones. From the analysis of different types of weathering occurring at two stone types employed for the construction of a heritage building, results can be summarized and discussed as follows (Figure 12).

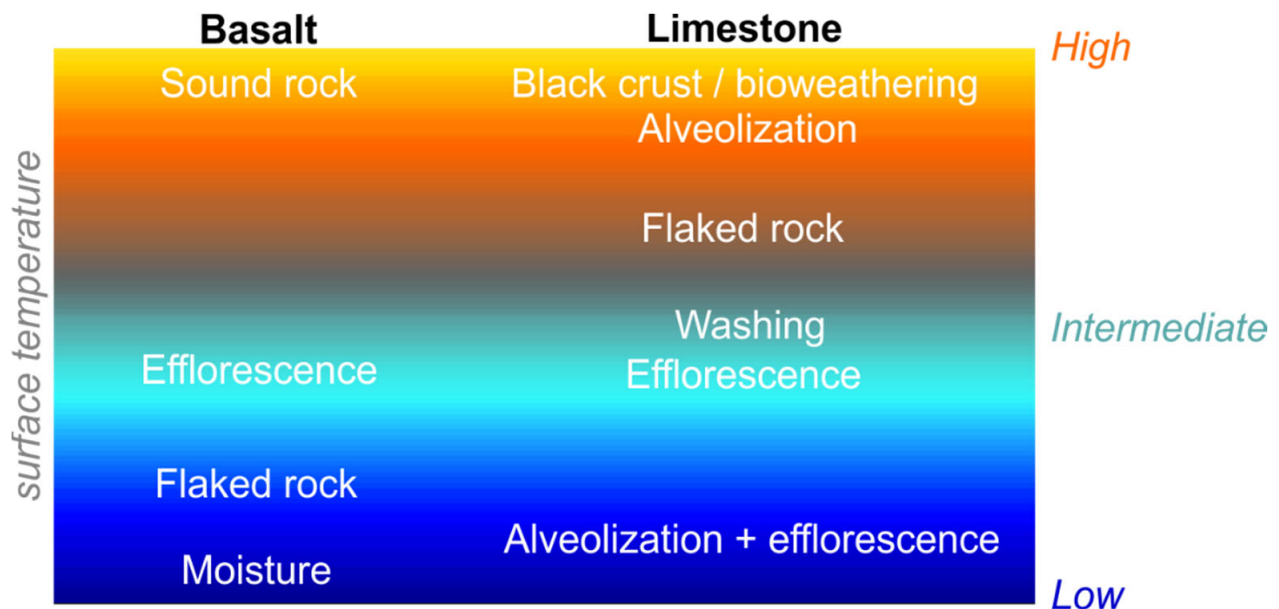


Figure 12. Schematic summary of the IRT qualitative ranges of temperature related to each weathering type observed under no solar radiation conditions and divided by rock type.

- (1) Efflorescence affects both studied rock types, and its occurrence leads to the formation of a light-color salt crystallization film on the stone surface. When the salt crystallization occurs within the rock structure (subflorescence), it leads to the progressive flaking of the rock surface, producing thin slices of rock material and progressively detaching from the rock. IRT allowed the detection of these weathering types thanks to key thermal contrasts. In particular, at basalts, the highest surface temperatures were found at the sound rock, where weathering did not occur, or at the bared rock portions, where flaking phenomena exposed the rock underneath the weathered surface. Intermediate surface temperatures were found where the salt crystallization film occurred, with the lowest values measured at its maximum thickness. Lowest surface temperatures were highlighted at the rock slices partly detached from the substratum due to flaking phenomena. Moreover, the cold regions affecting such rock portions can be regarded as flaking expansion areas, thus providing interesting information otherwise undetectable by the naked eye. The same considerations can be carried out for limestones, where efflorescence is often coupled with other weathering types and where flaking showed a slightly higher surface temperature than the surrounding area with efflorescence, unlike what was observed at the basaltic stereobates. This may be due to the presence of a heavier efflorescence around the limestone rock slice, which enhances the moisture absorption also due to the highest porosity of the rock type if compared to basalts.
- (2) Alveolar weathering affects only limestones, which represent the weaker rock type analyzed herein. Its occurrence was found localized in those rock regions overlaying the basaltic, more protruding strip, which favors the rain droplet rebound and their consequent impact and erosion on the limestone surface. Both stylobates of columns and the exposed wall of the western staircase are affected by this weathering type, which often occurs together with efflorescence and related flaking evidence. Their horizontal depth was estimated through the use of 3D photogrammetric models, which

allowed comparing the morphology of the alveolar structure to the IRT outcomes. In particular, when the alveolar structure is well defined, alveoli keep a high surface temperature due to the hollow morphology, while when efflorescence and/or flaking occurs within the cavity, its surface temperature is lowered.

- (3) Black crust and bioweathering were surveyed at limestones. The first one occurs in the most sheltered portions of the façade or where rain water did not play a washing effect on the rock surface. Bioweathering occurs in specific regions, especially in correspondence with signs of water flow. Due to the fact that surveys were performed during the dry season, the IRT aspect of these two weathering types is given by warm surface temperatures, arising from the darker color owned by the weathered rock portion. Therefore, in this specific case, the chromatic difference between the washed/unweathered rock and the darker films allows differentiating these elements by IRT.

It is underlined that the IRT results reported herein refer to surveys carried out under no direct solar radiation, which is considered the best time for IRT surveys for rock mechanics [16] and the absence of rain. Therefore, such results should be considered preliminary and more studies should be further performed to investigate the applicability of IRT to this specific field. Anyhow, IRT proved a reliable tool for a preliminary zonation and mapping of the weathering processes affecting natural stones. This gains relevance when quick studies are required, especially for preliminary assessments. IRT can be, indeed, employed to define restoration strategies and/or to prioritize interventions, as it allows a quick location of the problem, especially if located at high structural elements/building portion. The useful combination with 3D photogrammetry has a high potential for the quantitative estimation of weathering development in terms of the affected thickness of the stone. This would be useful also for monitoring purposes, both to study the weathering progression on heritage buildings and to verify the efficiency of restoration works already carried out.

Author Contributions: Conceptualization and methodology, G.P. and S.M.; visual analysis of selected stones and weathering characterization, A.B.; photogrammetry and IRT analyses, geomechanical analysis, data processing and interpretation, D.C., S.M. and G.P.; manuscript preparation, S.M. and G.P. All authors have read and agreed to the published version of the manuscript.

Funding: This research was financially supported by University of Catania, in the frame of “CH2V—Cultural Heritage Hazard and Vulnerability” project, Linea 2-PIACERI, granted to Giovanna Pappalardo.

Informed Consent Statement: Not applicable.

Data Availability Statement: Not applicable.

Acknowledgments: Physical-mechanical laboratory tests were carried out at the “Laboratorio di Geologia Applicata”, and the thermal camera was provided by “Laboratorio Analisi non Distruttive”, both belonging to the University of Catania, Department of Biological, Geological and Environmental Sciences.

Conflicts of Interest: The authors declare no conflict of interest.

References

1. Schiavon, N.; Chiavari, G.; Fabbri, D. Soiling of Limestone in an Urban Environment Characterized by Heavy Vehicular Exhaust Emissions. *Environ. Geol.* **2004**, *46*, 448–455. [[CrossRef](#)]
2. Lefèvre, R.A.; Ausset, P. Atmospheric Pollution and Building Materials: Stone and Glass. *Geol. Soc. Lond. Spec. Publ.* **2002**, *205*, 329–345. [[CrossRef](#)]
3. Montana, G.; Randazzo, L.; Mazzoleni, P. Natural and Anthropogenic Sources of Total Suspended Particulate and Their Contribution to the Formation of Black Crusts on Building Stone Materials of Catania (Sicily). *Environ. Earth Sci.* **2012**, *67*, 1097–1110. [[CrossRef](#)]
4. Winkler, E.M. Important Agents of Weathering for Building and Monumental Stone. *Eng. Geol.* **1966**, *1*, 381–400. [[CrossRef](#)]
5. Benavente, D. Role of Pore Structure in Salt Crystallisation in Unsaturated Porous Stone. *J. Cryst. Growth* **2004**, *260*, 532–544. [[CrossRef](#)]

6. Chastre, C.; Ludovico-Marques, M. Nondestructive Testing Methodology to Assess the Conservation of Historic Stone Buildings and Monuments. In *Handbook of Materials Failure Analysis*; Elsevier: Amsterdam, The Netherlands, 2018; pp. 255–294. [[CrossRef](#)]
7. Donato, A.; Randazzo, L.; Ricca, M.; Rovella, N.; Collina, M.; Ruggieri, N.; Dodaro, F.; Costanzo, A.; Alberghina, M.F.; Schiavone, S.; et al. Decay Assessment of Stone-Built Cultural Heritage: The Case Study of the Cosenza Cathedral Façade (South Calabria, Italy). *Remote Sens.* **2021**, *13*, 3925. [[CrossRef](#)]
8. Ercoli, L.; Megna, B.; Nocilla, A.; Zimbaro, M. Measure of a Limestone Weathering Degree Using Laser Scanner. *Int. J. Archit. Herit.* **2013**, *7*, 591–607. [[CrossRef](#)]
9. Casula, G. Experimental application of 3-d terrestrial laser scanning and acoustic techniques in assessing the quality of stones used in monumental structures. In Proceedings of the 4th International Conference on NDT, Chania, Greece, 11–14 October 2007.
10. Avdelidis, N.P.; Moropoulou, A. Applications of Infrared Thermography for the Investigation of Historic Structures. *J. Cult. Herit.* **2004**, *5*, 119–127. [[CrossRef](#)]
11. Mineo, S.; Pappalardo, G. InfraRed Thermography Presented as an Innovative and Non-Destructive Solution to Quantify Rock Porosity in Laboratory. *Int. J. Rock Mech. Min. Sci.* **2019**, *115*, 99–110. [[CrossRef](#)]
12. Pappalardo, G.; Mineo, S. Investigation on the Mechanical Attitude of Basaltic Rocks from Mount Etna through InfraRed Thermography and Laboratory Tests. *Constr. Build. Mater.* **2017**, *134*, 228–235. [[CrossRef](#)]
13. Pappalardo, G.; Mineo, S.; Calcaterra, D. Geomechanical analysis of unstable rock wedges by means of geostructural and infrared thermography surveys. *Ital. J. Eng. Geol. Environ.* **2017**, *1*, 93–101. [[CrossRef](#)]
14. Pappalardo, G.; Mineo, S.; Carbone, S.; Monaco, C.; Catalano, D.; Signorello, G. Preliminary Recognition of Geohazards at the Natural Reserve “Lachea Islet and Cyclop Rocks” (Southern Italy). *Sustainability* **2021**, *13*, 1082. [[CrossRef](#)]
15. Frodella, W.; Elashvili, M.; Spizzichino, D.; Gigli, G.; Adikashvili, L.; Vacheishvili, N.; Kirkitadze, G.; Nadaraia, A.; Margottini, C.; Casagli, N. Combining InfraRed Thermography and UAV Digital Photogrammetry for the Protection and Conservation of Rupestrian Cultural Heritage Sites in Georgia: A Methodological Application. *Remote Sens.* **2020**, *12*, 892. [[CrossRef](#)]
16. Pappalardo, G.; Mineo, S.; Zampelli, S.P.; Cubito, A.; Calcaterra, D. InfraRed Thermography Proposed for the Estimation of the Cooling Rate Index in the Remote Survey of Rock Masses. *Int. J. Rock Mech. Min. Sci.* **2016**, *83*, 182–196. [[CrossRef](#)]
17. Punturo, R.; Russo, L.G.; Giudice, A.L.; Mazzoleni, P.; Pezzino, A. Building Stone Employed in the Historical Monuments of Eastern Sicily (Italy). An Example: The Ancient City Centre of Catania. *Environ. Geol.* **2006**, *50*, 156–169. [[CrossRef](#)]
18. Bas, M.J.L.; Maitre, R.W.L.; Streckeisen, A.; Zanettin, B.; IUGS Subcommittee on the Systematics of Igneous Rocks. A Chemical Classification of Volcanic Rocks Based on the Total Alkali-Silica Diagram. *J. Petrol.* **1986**, *27*, 745–750. [[CrossRef](#)]
19. Tanguy, J.C. Les Éruptions Historiques de L’Etna: Chronologie et Localisation. *Bull. Volcanol.* **1981**, *44*, 585–640. [[CrossRef](#)]
20. Pappalardo, G.; Punturo, R.; Mineo, S.; Contrafatto, L. The Role of Porosity on the Engineering Geological Properties of 1669 Lavas from Mount Etna. *Eng. Geol.* **2017**, *221*, 16–28. [[CrossRef](#)]
21. DeWitt, D.P.; Nutter, G.D. *Theory and Practice of Radiation Thermometry*; Wiley: New York, NY, USA, 1988.
22. Baroň, I.; Bečkovský, D.; Míča, L. Application of Infrared Thermography for Mapping Open Fractures in Deep-Seated Rockslides and Unstable Cliffs. *Landslides* **2014**, *11*, 15–27. [[CrossRef](#)]
23. Fiorucci, M.; Marmoni, G.M.; Martino, S.; Mazzanti, P. Thermal Response of Jointed Rock Masses Inferred from Infrared Thermographic Surveying (Acuto Test-Site, Italy). *Sensors* **2018**, *18*, 2221. [[CrossRef](#)]
24. Junique, T.; Vazquez, P.; Thomachot-Schneider, C.; Hassoun, I.; Jean-Baptiste, M.; Géraud, Y. The Use of Infrared Thermography on the Measurement of Microstructural Changes of Reservoir Rocks Induced by Temperature. *Appl. Sci.* **2021**, *11*, 559. [[CrossRef](#)]
25. Mineo, S.; Pappalardo, G. Preliminary Results on the Estimation of Porosity in Intact Rock through InfraRed Thermography. *ROL* **2016**, *41*, 317–320. [[CrossRef](#)]
26. Mezza, S.; Vazquez, P.; Ben M’barek Jemai, M.; Fronteau, G. Infrared Thermography for the Investigation of Physical–Chemical Properties and Thermal Durability of Tunisian Limestone Rocks. *Constr. Build. Mater.* **2022**, *339*, 127470. [[CrossRef](#)]
27. Deng, N.-F.; Qiao, L.; Li, Q.; Hao, J.-W.; Wu, S. A Method to Predict Rock Fracture with Infrared Thermography Based on Heat Diffusion Analysis. *Geofluids* **2021**, *2021*, 6669016. [[CrossRef](#)]
28. Eyssautier-Chuine, S.; Mouhoubi, K.; Reffuveille, F.; Bodnar, J.-L. Thermographic Imaging for Early Detection of Biocolonization on Buildings. *Build. Res. Inf.* **2020**, *48*, 856–865. [[CrossRef](#)]
29. Korkanç, M.; Hüseyinca, M.Y.; Hatır, M.E.; Tosunlar, M.B.; Bozdağ, A.; Özen, L.; İnce, İ. Interpreting Sulfated Crusts on Natural Building Stones Using Sulfur Contour Maps and Infrared Thermography. *Environ. Earth Sci.* **2019**, *78*, 378. [[CrossRef](#)]
30. Paoletti, D.; Ambrosini, D.; Sfarra, S.; Bisegna, F. Preventive Thermographic Diagnosis of Historical Buildings for Consolidation. *J. Cult. Herit.* **2013**, *14*, 116–121. [[CrossRef](#)]
31. Balaras, C.A.; Argiriou, A.A. Infrared Thermography for Building Diagnostics. *Energy Build.* **2002**, *34*, 171–183. [[CrossRef](#)]
32. Thomachot-Schneider, C.; Gommeaux, M.; Lelarge, N.; Conreux, A.; Mouhoubi, K.; Bodnar, J.-L.; Vázquez, P. Relationship between Na₂SO₄ Concentration and Thermal Response of Reconstituted Stone in the Laboratory and on Site. *Environ. Earth Sci.* **2016**, *75*, 762. [[CrossRef](#)]
33. Mineo, S.; Pappalardo, G. Rock Emissivity Measurement for Infrared Thermography Engineering Geological Applications. *Appl. Sci.* **2021**, *11*, 3773. [[CrossRef](#)]
34. Yilmaz, H.M.; Yakar, M.; Yildiz, F. Documentation of Historical Caravansaries by Digital Close Range Photogrammetry. *Autom. Constr.* **2008**, *17*, 489–498. [[CrossRef](#)]
35. Pieraccini, M.; Guidi, G.; Atzeni, C. 3D Digitizing of Cultural Heritage. *J. Cult. Herit.* **2001**, *2*, 63–70. [[CrossRef](#)]

36. Dostal, C.; Yamafune, K. Photogrammetric Texture Mapping: A Method for Increasing the Fidelity of 3D Models of Cultural Heritage Materials. *J. Archaeol. Sci. Rep.* **2018**, *18*, 430–436. [[CrossRef](#)]
37. Yastikli, N. Documentation of Cultural Heritage Using Digital Photogrammetry and Laser Scanning. *J. Cult. Herit.* **2007**, *8*, 423–427. [[CrossRef](#)]
38. Lezzerini, M.; Antonelli, F.; Columbu, S.; Gadducci, R.; Marradi, A.; Miriello, D.; Parodi, L.; Secchiari, L.; Lazzeri, A. Cultural Heritage Documentation and Conservation: Three-Dimensional (3D) Laser Scanning and Geographical Information System (GIS) Techniques for Thematic Mapping of Facade Stonework of St. Nicholas Church (Pisa, Italy). *Int. J. Archit. Herit.* **2016**, *10*, 9–19. [[CrossRef](#)]
39. Randazzo, L.; Collina, M.; Ricca, M.; Barbieri, L.; Bruno, F.; Arcudi, A.; La Russa, M.F. Damage Indices and Photogrammetry for Decay Assessment of Stone-Built Cultural Heritage: The Case Study of the San Domenico Church Main Entrance Portal (South Calabria, Italy). *Sustainability* **2020**, *12*, 5198. [[CrossRef](#)]
40. Příkryl, R. Some Microstructural Aspects of Strength Variation in Rocks. *Int. J. Rock Mech. Min. Sci.* **2001**, *38*, 671–682. [[CrossRef](#)]
41. Pappalardo, G.; Mineo, S.; Monaco, C. Geotechnical Characterization of Limestones Employed for the Reconstruction of a UNESCO World Heritage Baroque Monument in Southeastern Sicily (Italy). *Eng. Geol.* **2016**, *212*, 86–97. [[CrossRef](#)]
42. Tugrul, A.; Zarif, I.H. Engineering Aspects of Limestone Weathering in Istanbul, Turkey. *Bull. Eng. Geol. Environ.* **2000**, *58*, 191–206. [[CrossRef](#)]
43. Sabatakakis, N.; Koukis, G.; Tsiambaos, G.; Papanakli, S. Index Properties and Strength Variation Controlled by Microstructure for Sedimentary Rocks. *Eng. Geol.* **2008**, *97*, 80–90. [[CrossRef](#)]
44. Viers, J.; Oliva, P.; Dandurand, J.-L.; Dupré, B.; Gaillardet, J. Chemical Weathering Rates, CO₂ Consumption, and Control Parameters Deduced from the Chemical Composition of Rivers. In *Treatise on Geochemistry*; Elsevier: Amsterdam, The Netherlands, 2014; pp. 175–194. [[CrossRef](#)]
45. Příkryl, R.; Melounová, L.; Vařilová, Z.; Weishauptová, Z. Spatial Relationships of Salt Distribution and Related Physical Changes of Underlying Rocks on Naturally Weathered Sandstone Exposures (Bohemian Switzerland National Park, Czech Republic). *Environ. Geol.* **2007**, *52*, 409–420. [[CrossRef](#)]
46. Young, A.R.M. Salt as an Agent in the Development of Cavernous Weathering. *Geology* **1987**, *15*, 962. [[CrossRef](#)]
47. Magee, A.W.; Bull, P.A.; Goudie, A.S. Chemical Textures on Quartz Grains: An Experimental Approach Using Salts. *Earth Surf. Process. Landf.* **1988**, *13*, 665–676. [[CrossRef](#)]
48. Nord, A.G. Efflorescence Salts on Weathered Building Stone in Sweden. *Geol. Föreningen Stockh. Förhandlingar* **1992**, *114*, 423–429. [[CrossRef](#)]
49. Peñas Castejón, J.M.; Maciá Sánchez, J.F.; Jiménez Medina, M.P.; Peñalver Martínez, M.J. Cyclical Salt Efflorescence Weathering: An Invisible Threat to the Recovery of Underground Mine Environment for Tourist Exploitation. *Environ. Earth Sci.* **2014**, *72*, 1901–1913. [[CrossRef](#)]
50. Harris, S.Y. *Building Pathology: Deterioration, Diagnostics, and Intervention*; Wiley: New York, NY, USA, 2001.
51. Siedel, H. Alveolar Weathering of Cretaceous Building Sandstones on Monuments in Saxony, Germany. *Geol. Soc. Lond. Spec. Publ.* **2010**, *333*, 11–23. [[CrossRef](#)]
52. Steiger, M. Crystal Growth in Porous Materials—I: The Crystallization Pressure of Large Crystals. *J. Cryst. Growth* **2005**, *282*, 455–469. [[CrossRef](#)]
53. La Russa, M.F.; Belfiore, C.M.; Fichera, G.V.; Mascalco, R.; Calabrò, C.; Ruffolo, S.A.; Pezzino, A. The Behaviour to Weathering of the Hyblean Limestone in the Baroque Architecture of the Val Di Noto (SE Sicily): An Experimental Study on the “Calcarea a Lumachella” Stone. *Constr. Build. Mater.* **2015**, *77*, 7–19. [[CrossRef](#)]
54. Occhipinti, R.; Stroschio, A.; Maria Belfiore, C.; Barone, G.; Mazzoleni, P. Chemical and Colorimetric Analysis for the Characterization of Degradation Forms and Surface Colour Modification of Building Stone Materials. *Constr. Build. Mater.* **2021**, *302*, 124356. [[CrossRef](#)]
55. Benavente, D.; de Jongh, M.; Cañaveras, J.C. Weathering Processes and Mechanisms Caused by Capillary Waters and Pigeon Droppings on Porous Limestones. *Minerals* **2020**, *11*, 18. [[CrossRef](#)]
56. Maldonado, L.; Veleza, L.; Díaz-Ballote, L. Characterization of Limestones for Building in the Yucatan Peninsula, Mexico. *Appl. Phys. A* **2011**, *103*, 1105–1110. [[CrossRef](#)]
57. Camuffo, D.; Del Monte, M.; Sabbioni, C. Origin and Growth Mechanisms of the Sulfated Crusts on Urban Limestone. *Water Air Soil Pollut.* **1983**, *19*, 351–359. [[CrossRef](#)]
58. Sabbioni, C.; Zappia, G. Atmospheric-Derived Element Tracers on Damaged Stone. *Sci. Total Environ.* **1992**, *126*, 35–48. [[CrossRef](#)]
59. Barca, D.; Belfiore, C.M.; Crisci, G.M.; La Russa, M.F.; Pezzino, A.; Ruffolo, S.A. A New Methodological Approach for the Chemical Characterization of Black Crusts on Building Stones: A Case Study from the Catania City Centre (Sicily, Italy). *J. Anal. At. Spectrom.* **2011**, *26*, 1000. [[CrossRef](#)]
60. Török, Á.; Licha, T.; Simon, K.; Siegesmund, S. Urban and Rural Limestone Weathering; the Contribution of Dust to Black Crust Formation. *Environ. Earth Sci.* **2011**, *63*, 675–693. [[CrossRef](#)]
61. Mitsos, D.; Kantarelou, V.; Palamara, E.; Karydas, A.G.; Zacharias, N.; Gerasopoulos, E. Characterization of Black Crust on Archaeological Marble from the Library of Hadrian in Athens and Inferences about Contributing Pollution Sources. *J. Cult. Herit.* **2022**, *53*, 236–243. [[CrossRef](#)]

62. Scheerer, S.; Ortega-Morales, O.; Gaylarde, C. Chapter 5 Microbial Deterioration of Stone Monuments—An Updated Overview. *Adv. Appl. Microbiol.* **2009**, *66*, 97–139. [[CrossRef](#)]
63. Mineo, S.; Pappalardo, G. Nondestructive Rock Porosity Estimation by InfraRed Thermography Applied to Natural Stones. *Constr. Build. Mater.* **2022**, *342*, 127950. [[CrossRef](#)]
64. Pappalardo, G.; Mineo, S. Study of Jointed and Weathered Rock Slopes Through the Innovative Approach of InfraRed Thermography. In *Landslides: Theory, Practice and Modelling*; Pradhan, S.P., Vishal, V., Singh, T.N., Eds.; Advances in Natural and Technological Hazards Research; Springer International Publishing: Cham, Switzerland, 2019; Volume 50, pp. 85–103. [[CrossRef](#)]
65. Pappalardo, G.; Mineo, S.; Imposa, S.; Grassi, S.; Leotta, A.; La Rosa, F.; Salerno, D. A Quick Combined Approach for the Characterization of a Cliff during a Post-Rockfall Emergency. *Landslides* **2020**, *17*, 1063–1081. [[CrossRef](#)]
66. Mineo, S.; Caliò, D.; Pappalardo, G. UAV-Based Photogrammetry and Infrared Thermography Applied to Rock Mass Survey for Geomechanical Purposes. *Remote Sens.* **2022**, *14*, 473. [[CrossRef](#)]